Room-temperature mixed spin state of Co3+ in Sr2Co0.02Ga0.98NbO6 double perovskite: combined NMR and EPR studies in a potential inorganic pigment

Maneesha Varghese, Struan Simpson, Gaynor Lawrence, Mathieu Duttine, Paula Sanz Camacho, Manuel Gaudon, Olivier Toulemonde

Room temperature mixed spin-state of Co^{3+} in $Sr_2Co_{0.02}Ga_{0.98}NbO_6$ double perovskite: combined NMR and EPR studies in a potential inorganic pigment

Maneesha Varghese[1], Struan Simpson[1,2], Gaynor Lawrence[1,2], Mathieu Duttine[1], Paula Sanz Camacho[1], Manuel Gaudon[1], Olivier Toulemonde[1*]

[1]*Univ. Bordeaux, CNRS, Bordeaux INP, ICMCB, UMR 5026, F-33600 Pessac, France*

[2]*The Chemistry Department, University of Aberdeen, Aberdeen AB24 3UE, Scotland*

Corresponding author email address: olivier.toulemonde@icmcb.cnrs.fr

Abstract

The structural and optical properties of the refractory oxides $Sr_2Co_xGa_{1-x}NbO_6$ (x=0 and 0.02) were investigated using X-ray powder diffraction, ^{93}Nb, ^{71}Ga and ^{59}Co Magic-Angle Spinning Nuclear Magnetic Resonance, Electron Spin Resonance and UV-vis-NIR absorption. A flux using $SrCl_2$ versus a ball milling strategy to stabilize rock salt ordered $Sr_2Co_xGa_{1-x}NbO_6$ (x=0 and 0.02) at low temperature was underlined. $Sr_2Co_{0.02}Ga_{0.98}NbO_6$ shows a tetragonal I*4/m* crystalline structure with a slight lattice distortion index in the range of 0.04. Combined spectroscopic studies further supported by UV-vis-NIR absorption analysis, definitively indicate an unusual mixed spin-state of Co^{3+} at room temperature in the $Sr_2Co_{0.02}Ga_{0.98}NbO_6$ double perovskite that might be of interest for pale brown inorganic pigments.

Introduction

Most of the refractory oxides[1] are insulating. However, it has been shown that slight composition changes can turn them to semi-conductor. Optical and/or photocatalysis properties over semi-conductor are nowadays among these that are widely studied. It is either to propose inorganic pigments for (smart) paintings or sensors devices when thermochromism is involved[2–6] or to apply the reaction to efficient utilization of solar energy for water splitting respectively. In those two technological fields, the control of the synthesis process is fundamental. Indeed, the characterization of the chemical nature of the lattice defects and its/their amounts are crucial to highlight the real driving force of the final properties. Interestingly, because of the spin state degree of freedom of Co^{3+}, cobaltates have been of interest due to the thermally induced spin-crossover phenomenon particularly in $LaCoO_3$[7–10] and solid solutions of the form $LaB'_{1-x}Co_xO_3$ (B' = Al, Ga)[11–13]. Spin-crossover is the phenomenon of changing the spin state of an ion by some external stimulus like temperature, pressure, irradiation of light or an applied magnetic field. With the change of the spin state, the material changes its color owing to the spin transition which is called X-chromism. This switching phenomenon have mostly been of research interest in d^4–d^7 transition metals in molecular complexes and coordination compounds. Observance of spin switching in octahedral complexes of d^4–d^7 occurs for a HS state (LS) when the ligand field strength is weaker (stronger) than the spin pairing energy.[14] When it comes to molecular complexes or coordination compounds, not a large palette of colors is available for the materials which show X-chromism.[11] However, X-chromic studies on oxides have shown a better palette of colors like the electrochromic study on WO_3[15–18], V_2O_5[19–24], photochromism in WO_3[25–28], piezo- and thermochromism on molybdates $AMoO_4$[29–31]. Co^{3+} (d^6) ion exists in 3 different spin states, namely low spin (LS) (S = 0; $t_{2g}^6e_g^0$), intermediate spin (IS) (S = 1; $t_{2g}^5e_g^1$) and high spin (HS) (S = 2, $t_{2g}^4e_g^2$). Interestingly, cobaltates have proven to be good photocatalysts[32,33] and the e_g^1 electronic configuration is responsible for driving the photocatalysis observed[34]. However, disputes about the existence of the IS spin state of Co^{3+} have been prevalent. IS Co^{3+} with an electronic configuration $t_{2g}^5e_g^1$ is a Jahn-Teller active ion and with sufficiently distorted octahedra, IS Co^{3+} can gain energy to become the ground state. This very point – that the distortion of octahedra might be the indicator to the existence of IS Co^{3+} in cobaltates – has been a sparring topic.[35–38]

The current study is put forward in that context, i.e., impact on the optical and/or chemical properties of a 3d transition metal element introduced in an insulating and diamagnetic double perovskite matrix. An in-depth study of the correlation between the average crystalline structure and their defects is proposed. Thus, herein, we explore the crystallographic, spectroscopic (combining Nuclear Magnetic Resonance (NMR) with Electron Paramagnetic Resonance (EPR)) and optical properties of $Sr_2Co_{0.02}Ga_{0.98}NbO_6$ synthesized using a flux (molten salt) method as previously detailed for Sr_2AlNbO_6[39]. First, the flux method interest is underlined with respect to ball milling assisted by ceramic solid-state synthesis. Then, an unusual mixed spin states of the cobalt is shown herein, the rate of which can be tuned by thermal treatments.

Methods

A. Synthesis

Undoped Sr_2GaNbO_6 samples were also synthesized starting with a ball milling process. Before the milling procedure, stoichiometric masses of $SrCO_3$, Ga_2O_3, and Nb_2O_5 were weighed on an analytical balance before being mixed and ground with a mortar and pestle. Two sets of powder combinations were prepared, one for each milling rate chosen. The powders were transferred to a grinding jar containing six 10 mm SiO_2 balls, and a small amount of distilled water was added so that a paste was formed. The mixtures were then placed in a Broyeur planetary Agate ball miller at either 300 rpm or 500 rpm for 30 minutes, with subsamples being obtained every 3 minutes to track the changes in particle size over the course of the milling programme. For the mixture milled at 500 rpm, preliminary results suggested that further milling could prove beneficial and so the mixture was further milled for another 30 minutes, this time taking subsamples every 10 minutes. After milling had been performed, small amounts of the samples milled at 300 rpm for 30 minutes and 500 rpm for 30 and 60 minutes were placed in alumina crucibles and heated to 900°C for 8 h under air (heating/cooling rate = 5°C/min); XRD patterns were obtained for all three samples after this heat treatment. The purpose of this was to identify which milling programme resulted in optimal formation of the desired phase. Furthermore, the sample milled at 500 rpm for 60 minutes was subsequently annealed again at various temperatures from 900°C to 1200°C for 8 h under O_2 (heating/cooling rate = 5°C/min) to see if the purity or crystallinity of the sample could be improved relative to the flux method; this also provided an opportunity to identify the optimum annealing temperature for the flux-synthesized samples. XRD patterns were obtained after heating to each temperature.

The Sr_2GaNbO_6 reference sample called (a) in the manuscript was prepared using the conventional solid-state route followed by annealing treatments (two 12 hour dwells at 1200 ℃ and a long anneal at 800 ℃ for 36 hour dwell time) on pelletized sample with intermediate grinding in a Broyeur planeteure agate ball miller.

$Sr_2Co_xGa_{1-x}NbO_6$ (x= 0.02) samples were prepared using a two-step synthesis. First, a flux (molten salt) method to stabilize the desired perovskite phase was carried out. $SrCO_3$ had been dried at 100°C before using it in the synthesis so as to remove the moisture. Stoichiometric amounts of high purity (99.99%) $SrCO_3$ (dried), Ga_2O_3, Nb_2O_5 and Co_3O_4 were ground along with $SrCl_2$ flux in a 2:1 flux:product ratio with a mortar with a pestle. The mixture was then transferred to a platinum crucible before being subjected to heat treatment for 8 hours under oxygen with a cooling rate of 5°C/min. After the initial thermal treatment, the resulting solid product was washed using distilled water acidified with few drops of HCl to remove the flux from the product. The washed sample was then collected on filter paper and dried in a furnace at 100°C overnight before being characterized. Secondly, two subsequent thermal treatments were carried out at 1200°C for 12 h under O_2 (heating/cooling rate = 5°C/min). High temperature

annealing was performed under a flow of O_2 to prevent the unwanted reduction of Nb^{5+} to Nb^{4+}. XRD patterns were obtained after each thermal treatment.

B. Structural, spectroscopic, optical studies

A PANalytical X'Pert Pro diffractometer equipped with an X'Celerator detector using Cu-$K\alpha_1$ radiation - Ge (111) monochromator had been used to perform the Powder X-Ray Diffraction (PXRD) measurements of the compounds. Rietveld refinement of the unit cell parameters was carried out using TOPAS software. Details of refinement are reported in the following sections.

Particle sizes for the ball milling investigations were measured via laser diffraction analysis, using a Malvern Mastersizer 2000 particle size analyser. Distilled water was used as a solvent and a refractive index of 1.5 was assumed. Particle sizes are reported as volume-equivalent sphere diameters. Prior to measurement, the samples were subjected to ultrasound to ensure any particulate aggregates were broken up as much as possible.

A Bruker ESP300E spectrometer operating at X-band frequency (9.54 GHz) was used to record the temperature dependent EPR powder spectra. The spectroscopic parameters used to obtain the reported spectra are microwave power of 10 mW, magnetic field modulation frequency of 100 kHz and amplitude of 1 mT and spectral resolution of 0.65 G/point. The spectrometer was calibrated (in magnetic field) using a reference sample of *DPPH* (g = 2.0036).

Single-pulse ^{93}Nb (I = +9/2) MAS NMR spectra were recorded on a Bruker Avance III (7.05 T magnet 300 MHz solid-state spectrometer) using a standard Bruker 2.5 mm MAS probe with a 30 kHz typical spinning frequency. A short pulse length of 1.26 μs corresponding to a $\pi/20$ pulse and an optimized recycle delay time of 0.5 s was used. Saturated solution of $NbCl_5$ (in CH_3CN) was used as reference sample for the ^{93}Nb shifts (expressed in ppm). ^{71}Ga (I = –3/2) MAS NMR spectra were recorded on a Bruker Avance III (11.7 T magnet 500 MHz solid-state spectrometer) using a standard Bruker 2.5 mm MAS probe with a 30 kHz typical spinning frequency. A Hahn echo pulse sequence ($\pi/2 - \tau - \pi$) synchronized at one rotor period (τ = 33.33μs) with a $\pi/2$ pulse length of 2 μs and an optimized recycle delay time of 0.5 s was used. 1M solution of $Ga(NO_3)_3$ was used as reference sample for the ^{71}Ga shifts (expressed in ppm). ^{59}Co (I = +7/2) MAS NMR spectra were recorded on a Bruker Avance III (11.7 T magnet 500 MHz solid-state spectrometer) using a standard Bruker 2.5 mm MAS probe with a 30 kHz typical spinning frequency. A Hahn echo pulse sequence ($\pi/2 - \tau - \pi$) synchronized at one rotor period (τ = 33.33μs) with a $\pi/2$ pulse length of 2 μs and an optimized recycle delay time of 0.2 s was used. 0.1M solution of $K_3[Co(CN)_6]$ was used as reference sample for the ^{71}Ga shifts (expressed in ppm).

UV-vis-NIR diffuse reflectance spectra were recorded using Agilent Cary 5000 spectrophotometer in the wavelength range of 200 nm – 1000 nm at room temperature. A step size of 1 nm was used for 200 nm – 800 nm range and 2 nm for 800 nm – 1000 nm range. Halon was used as a white reference to calibrate the spectrometer.

Results & Discussion

A. Sr_2GaNbO_6 stabilization using a milling procedure

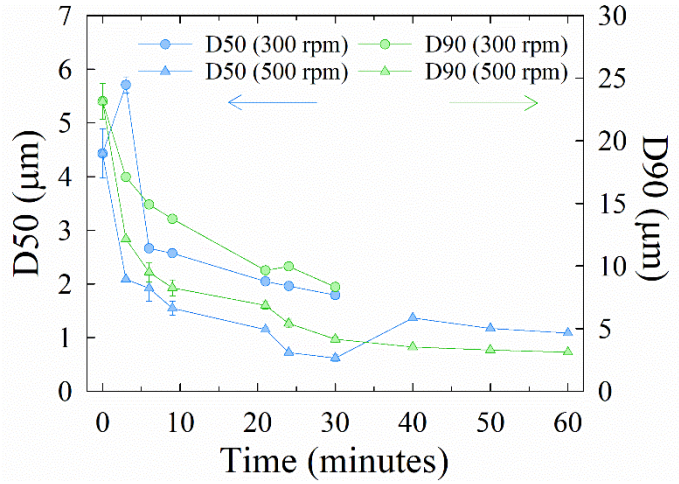

Fig. 1. D50 (blue) and D90 (green) values obtained for samples milled at 300 (circles) and 500 (triangles) rpm.

For samples milled at 300 rpm and 500 rpm, D50 and D90 values are displayed in Fig. 1 and represent the diameters below which 50% or 90% of all particles are found, respectively. After 30 minutes, the 500 rpm milling rate is clearly more effective at reducing the particle size. The D90 values smoothly decrease with increased milling time, as expected. However, the D50 values for both milling rates show abrupt variations until 30 minutes of milling, suggesting the particle size distributions remain inhomogeneous prior to this point. A comparison of the size distributions between the two milling rates is provided in Fig. 2. Milling for 30 minutes at 300 rpm produced two broad particle size distributions centered around 0.9 μm and 6 μm, showing the sample is still inhomogeneous after this milling time. Similarly, milling for 30 minutes at 500 rpm results in three sharp distribution peaks centered around 0.2 μm, 0.7 μm, and 2 μm. These peaks are centered at smaller sizes compared to the 300 rpm procedure, reflecting the decreased particle sizes obtained. Further milling was only attempted for the 500 rpm procedure to determine whether a more homogeneous distribution could be achieved. Further milling for an additional 30 minutes dramatically improves sample homogeneity, as shown by the single broad peak centered around 1 μm. The particle sizes then clearly converge towards 1 μm after 60 minutes; this result reflects the plateau in D50 and D90 values observed after this time. Overall, these results suggest milling at 500 rpm for 60 minutes was the best procedure purely in terms of obtaining small and homogeneous particle sizes.

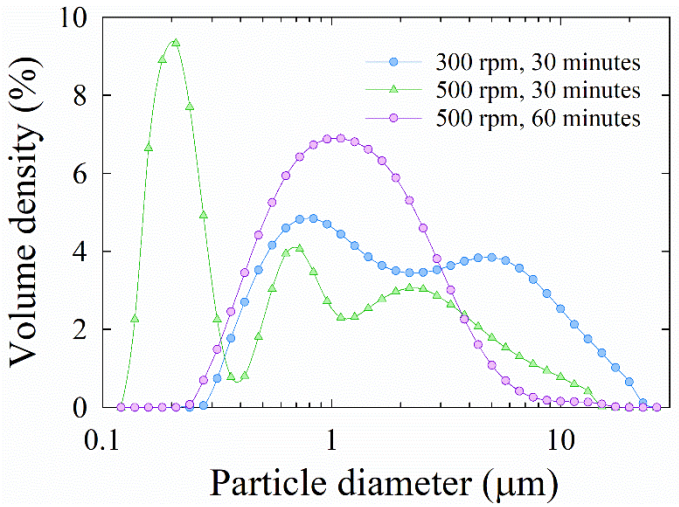

Fig. 2. Particle size distributions for samples milled at 300 rpm and 500 rpm.

Samples obtained after milling at 300 and 500 rpm were then subjected to an initial heating at 900 °C for 8 h. XRD patterns recorded after each initial heat are given in Fig. 3. The sample milled at 500 rpm after 60 minutes shows the most intense peaks corresponding to the expected perovskite-type reflections, one of which is highlighted as an example in the inset. However, each milling procedure tends to result in the formation of undesired secondary phases after their first heat treatment corresponding to strontium niobates such as $Sr_5Nb_4O_{15}$; furthermore, there are signs of unreacted starting materials (e.g. XRD peaks of $SrCO_3$ at 2θ values 25° and 26°). Therefore, further heat treatments were required in order to improve the formation of desired perovskite phase. Interestingly, the sample milled at 500 rpm for 30 minutes contains peaks in the XRD pattern that are not seen in the other two traces – an example of this can be seen in the inset of Fig. 3, where there seems to be at least two broad additional peaks (at ~30.5° and ~31.5°). Given the inhomogeneous particle sizes after this milling procedure, this is likely the cause of the observed discrepancies. The sample milled for 500 rpm after 60 minutes was then re-heated at 900°C for another 8 h to see if the purity could be further improved. These results are compared to a flux-synthesized sample in the following section.

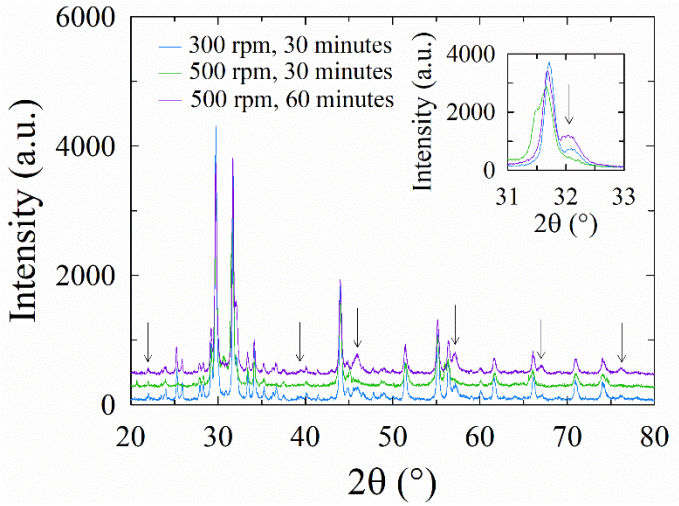

Fig. 3. XRD patterns of ball-milled samples at different rotations per minute and time; the inset highlights the (220) fundamental perovskite peak corresponding to the desired phase, while the arrows in the main figure indicate additional weak reflections consistent with the desired cubic perovskite phase.

B. Sr_2GaNbO_6 stabilization at 900°C: Flux and/or ball milling strategy

Fig. 4 displays the XRD pattern obtained after reheating the ball-milled sample (500 rpm for 60 minutes) for another 8 h at 900°C. This second heating step clearly improved the purity of the final product, though some small impurities (i.e., $Sr_5Nb_4O_{15}$) remain. Additional heating procedures at higher temperatures did not remove these impurities. For comparison, the XRD pattern for a flux-synthesized sample heated at 900°C for 8 h is also shown in Fig. 4. A single-phase sample is obtained after only one heating step at 900°C, demonstrating the superiority of flux synthesis method in preparing the phase pure Sr_2GaNbO_6 matrix. It was also investigated to see if it made sense to combine the two methods – that is, perform ball-milling on the starting materials before combining them with the flux and heating at high temperatures. Doing so may allow the phases that are introduced during the ball-milling procedure to be washed out with the flux. Fig-SI-1 provides a comparison between the XRD patterns recorded for a sample synthesized in this fashion with a sample synthesized using just the flux method – additional peaks are observed which do not correspond to the impurities previously observed. No match could be found to known compounds when the peaks were cross-referenced with a database, but since they do not correspond to the desired phase and are inconsistent with the expected positions of B-site ordering peaks, they are most likely impurities. It was therefore concluded that combining the two methods does not appear to result in any additional benefits over the flux method.

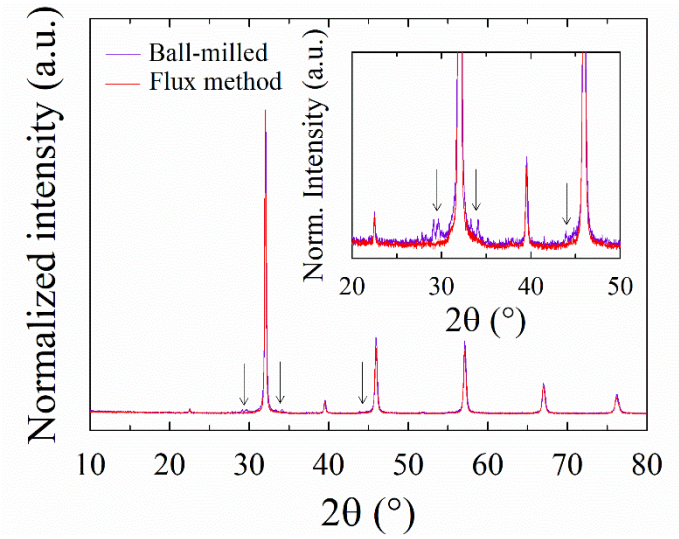

Fig. 4. Comparison of the XRD patterns obtained for samples synthesized via the ceramic method and flux method. The inset and arrows highlight the additional weak impurities observed in the ball-milled sample.

Consequently, it is clear from our study that the flux method is superior in forming phase pure Sr_2GaNbO_6, hence synthesis of the Co-doped samples was performed using this method. The further sample stabilization of the cobalt doped sample was done first using only the $SrCl_2$ flux with subsequent annealing processes to improve the B-site cation ordering.

C. Structural study: Room temperature Powder X-Ray Diffraction of $Sr_2Co_{0.02}Ga_{0.98}NbO_6$

The room temperature (RT) PXRD patterns were collected using the diffractometer and the data collection conditions as discussed in the experimental section. The collected RT PXRD patterns are shown in Fig. 5. (a), (b), (c) and (d) are marked for the samples which were undoped Sr_2GaNbO_6, Co-doped Sr_2GaNbO_6 prepared using flux method, and after first annealing and second annealing at 1200°C, respectively. The second annealing was performed on a pelletized sample. There was small trace of impurity observed in the samples, but as the impurity phase peaks are not much in intensity in the observed PXRD (in Fig. 5), it was hard to identify the impurity phase even the peak positions suggest the same phase that observed just after the ball milling procedure. Nevertheless, the ordering coherent length was found to be increased with the annealing processes which can be clearly seen from the inset of Fig. 5. The full width at half maximum (FWHM) of (111) superstructure peak (at ~19°) decreases from sample a to d giving the information about the ordering of B-site cations that the more sharp (less FWHM) superstructure peak is, the more B-site cation ordering is.[40]

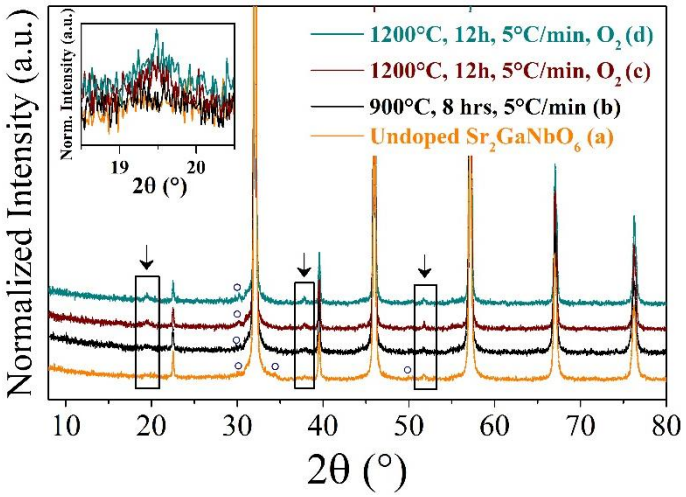

Fig. 5. Room temperature X-ray diffraction patterns of the Sr_2GaNbO_6 and $Sr_2Co_{0.02}Ga_{0.98}NbO_6$ double perovskites prepared to study the annealing effect. (a) is Sr_2GaNbO_6 and (b) is the $Sr_2Co_{0.02}Ga_{0.98}NbO_6$ sample prepared using flux method and (c) & (d) samples were obtained after consecutive annealing processes thereafter. The inset shows the superstructure peak ~19°.

For the purpose of refining X-ray diffraction pattern using Rietveld refinement[41] method to find out the crystal symmetry of the sample after annealing processes (sample d), the $K\alpha_1$ data collection was performed. As the high angle peaks were asymmetric in the RT PXRD ($K\alpha_1$) and with the charge difference between Ga^{3+} & Nb^{5+} is two (partial ordering is expected[39,42,43]), I4/m space group with a fractional occupancy of Ga & Nb octahedra approach was implemented for the structure refinement. The observed PXRD pattern, calculated pattern using I4/m and the difference patterns are shown in Fig. 6 along with the Bragg reflections for the I4/m space group marked with | markers. The asymmetry in the high angle peak (~102.5°) is shown in the inset of Fig. 6. There were two assumptions made *a priori* to the refinement: (1) Co^{3+} occupied Ga^{3+} site as desired, (2) the content of cobalt in the final product experimentally produced is equal to the targeted one, i.e., x = 0.02. Assumption 1 was made based on the ionic radii of HS Co^{3+}, LS Co^{3+}, Ga^{3+}, Nb^{5+} which are 0.61 Å, 0.545 Å, 0.62 Å, 0.64 Å and HS/LS Co^{3+} would go in the smaller radii site (Ga^{3+}) than in the higher radii site (Nb^{5+}). These assumptions were justified based on the NMR and EPR results, as discussed later. Hence, the fractional occupancy of Co^{3+} was kept constant as 0.02 during the refinement. The original Ga^{3+} site (0.5, 0.5, 0) have 0.02 parts occupied by Co^{3+} fractionally, *y* parts fractionally occupied by Ga^{3+} and 1–*y*–0.02 parts fractionally occupied by Nb^{5+}. And the original Nb^{5+} site (0, 0, 0) will have *y*–0.16 parts of total occupancy for Nb^{5+}, the rest 1–*y*–0.16 parts fractionally occupied by Ga^{3+}. The z parameter of O1 site was kept constant at 0.25 as freeing this parameter did not change the quality of the fit. Rietveld refinement results are tabulated in Table. 1 and the crystal structure deduced from the Rietveld refinement is shown in Fig. 7a & Fig. 7b.

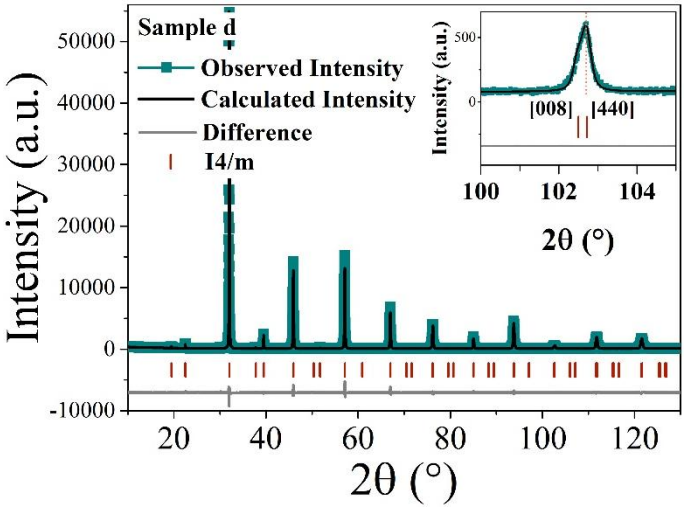

Fig. 6. Observed room temperature powder X-ray diffraction pattern (cyan), calculated diffraction pattern using I4/m space group with Rietveld refinement (black) and difference curve between the observed and calculated diffraction patterns (grey) along with the Bragg reflections for the I4/m space group (| markers) of $Sr_2Co_{0.02}Ga_{0.98}NbO_6$. Inset shows the asymmetric superstructure peak at ~102.5°. The dashed line through the peak in the inset is for the reader to easily realize the asymmetry of the peak.

Site	Np	x	y	z	Atom	Occupancy	B_{iso} (Å^2)
I4/m; a = 5.579 (1) Å, c = 7.902 (1) Å Rwp = 9.92 and χ^2 = 1.65							
Sr	4	0	0.5	0.25	Sr^{2+}	1	0.848 (11)
Ga	2	0.5	0.5	0	Ga^{3+}	0.748 (10)†	0.29 (3)††
					Nb^{5+}	0.232 (10)†	0.29 (3)††
					Co^{3+}	0.02	0.29 (3)††
Nb	2	0	0	0	Nb^{5+}	0.768 (10)⋆	0.17 (2)⋆⋆
					Ga^{3+}	0.232 (10)⋆	0.17 (2)⋆⋆
O1	4	0	0	0.25	O^{2-}	1	0.1 (2)
O2	8	0.267 (1)	0.237 (2)	0	O^{2-}	1	1.24 (13)

Table. 1. Crystal structure of $Sr_2Co_{0.02}Ga_{0.98}NbO_6$ double perovskites acquired from PXRD Rietveld refinement using TOPAS. $^{\dagger},^{\dagger\dagger},^{\star},^{\star\star}$ indicate that there were constraints imposed: (a) †Occupancy of Ga^{3+} + Occupancy of Co^{3+} + Occupancy of Nb^{5+} = 1 and *Occupancy of Nb^{5+} + Occupancy of Ga^{3+} = 1, (b) $^{\dagger\dagger},^{\star\star}$ Beq at these sites were constrained to be equal. Errors are shown in brackets.

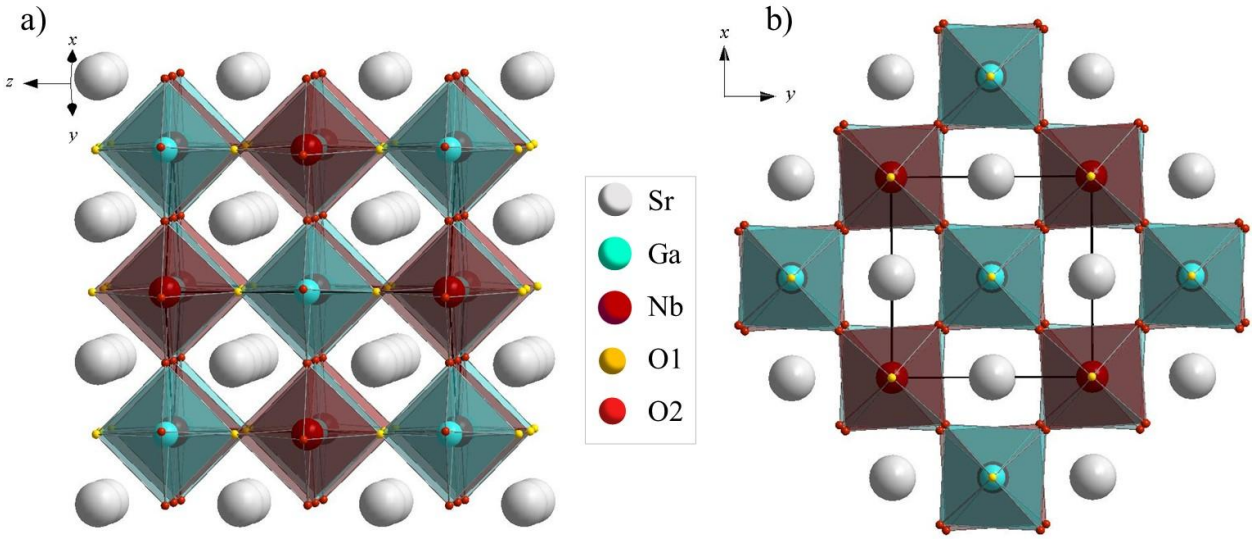

Fig. 7. Crystal structure of $Sr_2Co_{0.02}Ga_{0.98}NbO_6$ (a) showing ordering of the Ga/Nb octahedra and (b) octahedral tilting ($a^0a^0c^-$ Glazer notation[44]) when viewed along z-axis.

Bond distance (Å)	
Ga – O1	1.975 (×2)
Ga – O2	1.958 (8) (×4)
Nb – O1	1.975 (×2)
Nb – O2	1.994 (8) (×4)
Bond angle (°)	
<Ga – O1 – Nb>	180
<Ga – O2 – Nb>	173.2 (5)

Table. 2. Bond distances and bond angle deduced from structure refinement of $Sr_2Co_{0.02}Ga_{0.98}NbO_6$ with errors shown in brackets.

The octahedral tilting can be surmised from Table. 2 which shows the bond distances and the bond angle (angle of tilting). There are two oxygen positions, equatorial oxygen position marked O1 and axial oxygen position marked O2. The Ga^{3+} octahedra is compressed along the axial oxygen direction while Nb^{5+} octahedra is elongated (see Table. 2). The octahedral distortion parameter, Δd can be calculated using the following equation, $\Delta d = \frac{1}{6}\sum_{n=1}^{6}[d_n - d/d]^2$ where d

is the mean B – O bond distance and d_n is the individual B – O bond distances.[45] For GaO_6 octahedra, $\Delta d = 1.66 \times 10^{-5}$ and for NbO_6 octahedra, $\Delta d = 2.03 \times 10^{-5}$. It can be realized that the Nb octahedra is slightly more distorted than the Ga octahedra. The lattice distortion index, D (%) can be calculated as $D = \frac{1}{3}\sum_{n=1}^{3} 100 \times [(a_n - \langle a \rangle)/\langle a \rangle]$ where a_n is the individual lattice parameter converted to the equivalent primitive lattice parameter (a_p) and is calculated from the lattice parameters obtained from the PXRD refinement ($a_p \cong a/\sqrt{2} \cong b/\sqrt{2} \cong c/2$)[42] and $\langle a \rangle$ is the average of all a_n.[46] The reported D for Sr_2GaNbO_6 is 0.07%[47] whereas for $Sr_2Co_{0.02}Ga_{0.98}NbO_6$ (sample d) under study, D = 0.04%. The lattice parameter is less distorted when Ga was substituted with Co which in turn indicates that the Co substituted double perovskite is closer to the cubic symmetry than the undoped Sr_2GaNbO_6 double perovskite. Furthermore, the distortion of the octahedra is along the z-axis which is only visible when viewed in the xy-plane (Fig. 7b).

The degree of B-site cation ordering can be calculated using an order parameter, S and S = 2z–1 (where z is the highest fractional occupancy between B and B' cations)[42,48] and was obtained as 0.54. S = 0 corresponds to the disordered perovskite and S = 1 to the completely ordered double perovskite.[42] Though the lattice distortion index was lower for the Co-doped double perovskite under study (sample d), the cation ordering parameter, S for undoped Sr_2GaNbO_6 double perovskite which is S = 0.57 is not far from the Co-doped double perovskite. Therefore, even though the ordering was not improved, surprisingly, Co substitution helped the cubic cell of $Sr_2Co_{0.02}Ga_{0.98}NbO_6$ double perovskite to be formed in a crystal symmetry closer to cubic symmetry than in Sr_2GaNbO_6 double perovskite.

Due to poor contrast between the scattering factors of cobalt and gallium ions, the RT PXRD pattern refinement is proposed with the assumption that cobalt ion occupy only one crystalline site of the double perovskite. To support the assumption, Nuclear Magnetic Resonance (NMR) and Electron Paramagnetic Resonance (EPR) as local probes were carried out.

D. Spectroscopic study

I. Room temperature NMR

Nuclear Magnetic Resonance (NMR) spectroscopy is used for detecting the diamagnetic species as well. In the double perovskites under study, $Sr_2Co_{0.02}Ga_{0.98}NbO_6$ has three expected diamagnetic ions, i.e., LS Co^{3+}, Nb^{5+}, Ga^{3+} ions and for the reference sample, Sr_2GaNbO_6, two diamagnetic ions (Nb^{5+} and Ga^{3+}).

Fig. 8a & Fig. 8b show the ^{93}Nb, ^{71}Ga RT MAS NMR respectively of Sr_2GaNbO_6 reference sample noted (a). A main peak with asymmetry attributing from the site/anti-site disorder is observed in ^{93}Nb MAS NMR spectra of Sr_2GaNbO_6 double perovskite (see Fig. 8a). In ^{71}Ga MAS NMR spectra, the broad tail towards the low chemical shift values accounts for the site/anti-site disorder as well.[49,50] In addition, even if small traces of unreacted Ga_2O_3 or unknown gallium rich secondary phase can not be ruled out to explain the feature at 36 ppm, such feature also supports octahedral faults as oxygen vacancies[51,52] (explained later using EPR

spectra). However, it is not related to tetrahedral Ga site as the tetrahedral site gives a NMR signal ~100 ppm[53,54].

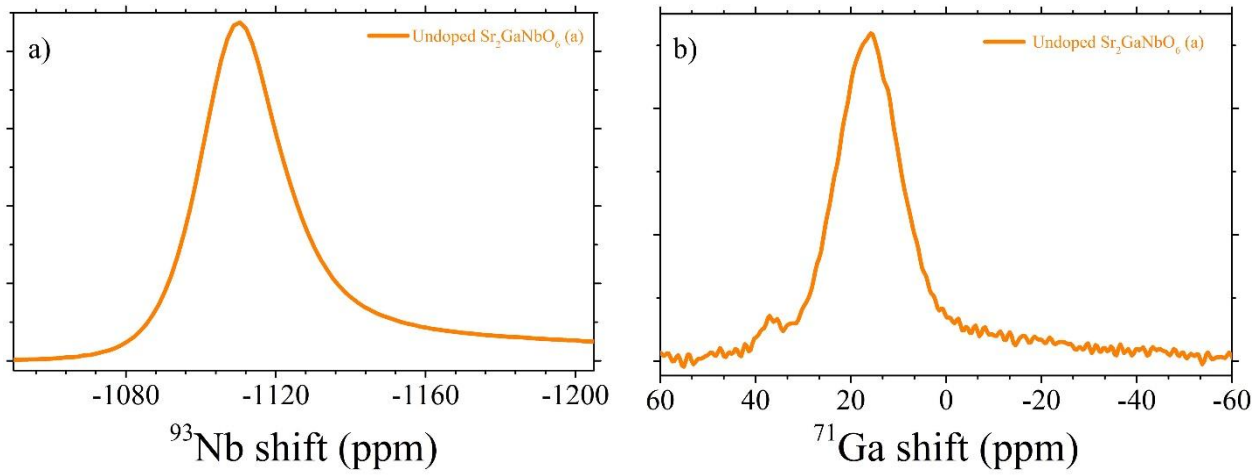

Fig. 8. (a) ^{93}Nb and (b) ^{71}Ga MAS NMR spectra of Sr_2GaNbO_6 double perovskite (sample a)

Fig. 9a, Fig. 9b & Fig. 9c show the ^{93}Nb, ^{71}Ga and ^{59}Co RT MAS NMR spectra respectively of Co-doped Sr_2GaNbO_6 compounds synthesized using flux method with respect to the thermal treatments along with the reference sample. The spectral intensity increases with respect to the consecutive thermal treatments and the peaks full width half maxima decrease as seen on all the proposed insets. It is a clear indication of the site/anti-site disorder decrease with the successive thermal treatments. Furthermore, ^{93}Nb NMR signal looks different than the ^{71}Ga and ^{59}Co NMR spectra. The difference in ^{93}Nb NMR from the ^{71}Ga and ^{59}Co NMR spectra and the similarity in the ^{71}Ga and ^{59}Co NMR favors the previous assumption of Co^{3+} being substituted at the Ga^{3+} site than to have been equally distributed in both the Ga^{3+} and Nb^{5+} sites. And, as can be seen from Fig. 9a that the ^{93}Nb MAS NMR of Sr_2GaNbO_6 double perovskite has the same spectra as of the $Sr_2Co_{0.02}Ga_{0.98}NbO_6$ double perovskite, it can be concluded that the broadened tail towards the low chemical shift values is not coming from the influence of Co^{3+} environment, but rather from a cation disorder. Additionally, the ^{93}Nb MAS NMR can be deconvoluted to two Gaussian main peaks and a broad tail as can be seen in Fig. S2 (a). This supports the site/anti-site distribution as seen from PXRD refinement result. Furthermore, there could be two possibilities for the interaction of probing species with its chemical environment, i.e., either with the next nearest neighbors or with the next-to-next nearest neighbors. Assuming complete ordering and considering ^{93}Nb MAS NMR spectra, there is only a weak and broad signal (sum of site/anti-site disordering components along with a tail) that would suggest the environment probed around a NbO_6 octahedra is uniform and that ought to be another NbO_6 octahedra as the neighboring interacting species, i.e., the interaction is between the probed species and the next-to-next nearest neighbors.

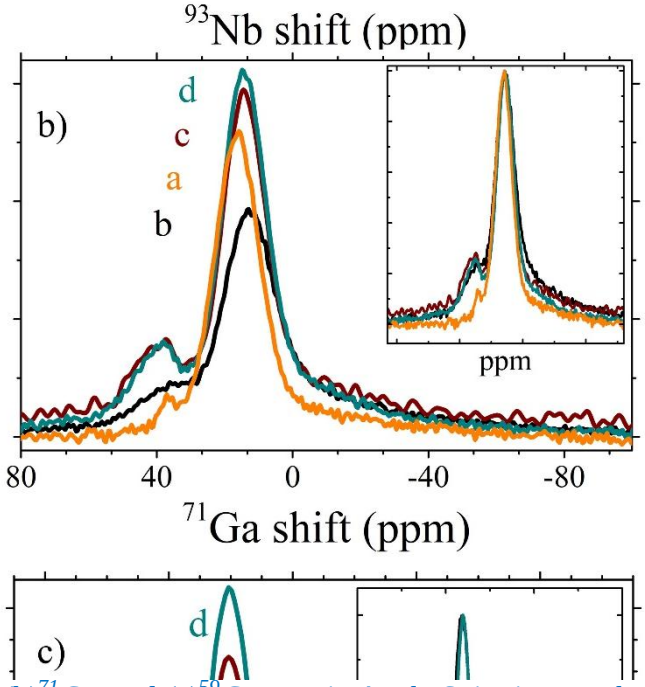

Fig. 9. Room temperature (a)^{93}Nb, (b)^{71}Ga and (c)^{59}Co Magic Angle Spinning Nuclear Magnetic Resonance spectra of $Sr_2Co_{0.02}Ga_{0.98}NbO_6$ prepared by flux method and post-annealing processes. Inset of each subfigure (^{93}Nb, ^{71}Ga, ^{59}Co MAS NMR spectra) show the normalized intensity and at chemical shifts shifted to a common center. In each figure, a, b, c, d corresponds to Sr_2GaNbO_6, $Sr_2Co_{0.02}Ga_{0.98}NbO_6$ prepared via flux method and two subsequent annealing treatments respectively.

For cobalt doped compounds, ^{71}Ga and ^{59}Co MAS NMR were additionally used to locally probe the distribution of Ga/Co environments in the samples under study at a local scale as pointed out. For this purpose, ^{71}Ga and ^{59}Co MAS NMR spectra deconvolution are given in Fig. S2 (b), (c). Interestingly, deconvolution of both the spectra gave similar number of subpeaks. Additionally, as shown in Fig. S2 (c), (d), (e) the deconvoluted ^{71}Ga NMR spectra of sample b & c has more environments than in the sample d with the number of subpeaks (at the low chemical shift values) getting reduced with annealing treatments. Sample b and d have the subpeak centers located at almost same chemical shift values, but sample b was deconvoluted to more peaks (more different environments) than sample d. This confirms the ordering improvement with the annealing in the studied double perovskite. This is bolstered by the PXRD data as previously seen by an increasing effect of ordering with the annealing. For ^{59}Co and ^{71}Ga MAS NMR spectra, the spectra do not show uniformity in its nature which further suggest that the interactions are between next-to-next nearest neighbors, i.e., either a GaO_6 or CoO_6 octahedra. Hence the chemical environment around Ga^{3+} / Co^{3+} has been proposed with the main peak coming from the twelve next-to-next nearest neighbors and the subpeaks accounting to the ($Ga_{12-n}Co_n$) distribution ($1 \leq n \leq 12$) with a possible mix of LS and IS/HS Co^{3+}.

The probability calculation for the structure determination of $Sr_2Co_{0.02}Ga_{0.98}NbO_6$ double perovskite was carried out to support the hypothesis put forth from the initial analysis of MAS NMR spectra. As samples a and d show the same intensity for the normalized asymmetric feature towards the low chemical shift values as shown in the inset, the statistical calculations were made considering only the high chemical shift values. There are twelve next-to-next nearest neighbors for Ga/Co octahedra. So, the individual probability to find cobalt atom around Co octahedra will depend on the Co substitution content, i.e., p = 0.02. Thus, by using binomial probability law, the probability (P) to find k cobalt atoms among n = 12 neighbors can be given as:

$$\mathrm{P} = \binom{n}{k} p^k (1-p)^{n-k}; 1 \leq k \leq 12 \,\&\, n = 12$$

The calculated probability and the intensity of the subpeaks at the high chemical shift values matches, as shown in Fig. 10 for ^{59}Co MAS NMR, and approves the hypothesis of $Ga_{12-n}Co_n$ around the Co octahedra. This indicates that by correlating both the measured ^{93}Nb and ^{71}Ga NMR spectra it can be said that the Co^{3+} is more likely to be substituted at the Ga^{3+} site. However, as the statistical calculation was carried out using Co substitution content (x=0.02) and by not distinguishing between the LS and HS/IS Co^{3+} (the presence of which is confirmed from EPR spectroscopy), the actual probability distribution must involve more than a binomial probability distribution. This perplexity along with four different types of neighbors around Ga/Co octahedra namely Ga, Nb, LS Co^{3+} and HS/IS Co^{3+} (originating from the partial disordering in the sample) makes the probability calculation for the full structure determination an intricate task outside the scope of this article.

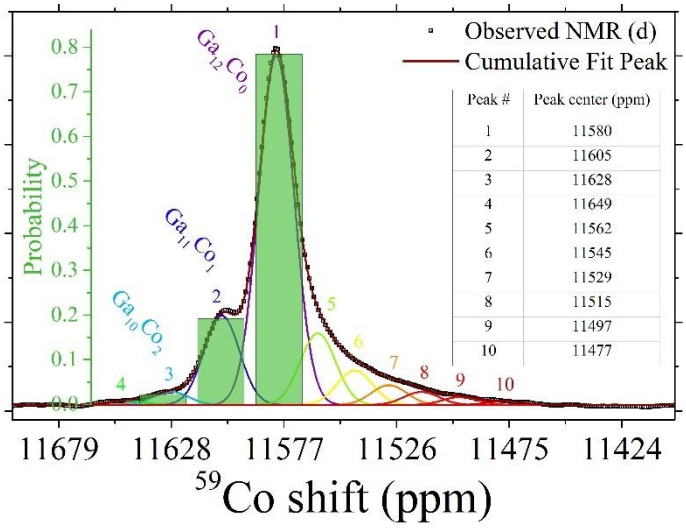

Fig. 10. Deconvoluted ^{59}Co MAS NMR spectra of $Sr_2Co_{0.02}Ga_{0.98}NbO_6$ (sample d) double perovskite along with the probability calculated (green bar graph) and the environments marked within.

Consequently, the assumption of Co^{3+} being mainly substituted at the Ga^{3+} crystallographic site as desired is confirmed from the correlated analysis of ^{71}Ga and ^{93}Nb NMR spectra along with

the statistical analysis of ^{59}Co NMR even if there is any anti-site as supported by the cationic distribution in the double perovskite under study. Also, from the observance of a ^{59}Co NMR spectrum, the presence of LS Co^{3+} in the studied samples is confirmed. As the deconvoluted ^{59}Co NMR has more subpeaks towards the low chemical shift and having the same number of subpeaks towards the high chemical shift in comparison to ^{71}Ga NMR, the local environment around Ga^{3+} has less different environments than Co^{3+}. Also, the decrease in subpeak numbers going from sample b to d indicates more ordering with annealing treatment.

II. Temperature dependent EPR spectroscopy

To cross check our NMR study, temperature dependent EPR spectroscopy were carried out allowing to complementarily probe the paramagnetic species being of great interest to follow the IS/HS Co^{3+} decrease with annealing procedure. The EPR spectra collected at RT and at 5 K for $Sr_2Co_{0.02}Ga_{0.98}NbO_6$ is shown in Fig. 11a & Fig. 11b respectively. There are two/three different g-values observed in the collected EPR spectra at RT and 5 K.

The RT EPR signals match with previous report for $LaCoO_3$ perovskites[55,56]. Interestingly, the broad signal at g~5.8 observed for sample b in Fig. 11a is almost vanished following a first thermal treatment to give rise in sample c and d. In parallel, the g~1.98 signal significantly increases in intensity when the experimental conditions are adjusted to improve the B/B' ordering reaction.

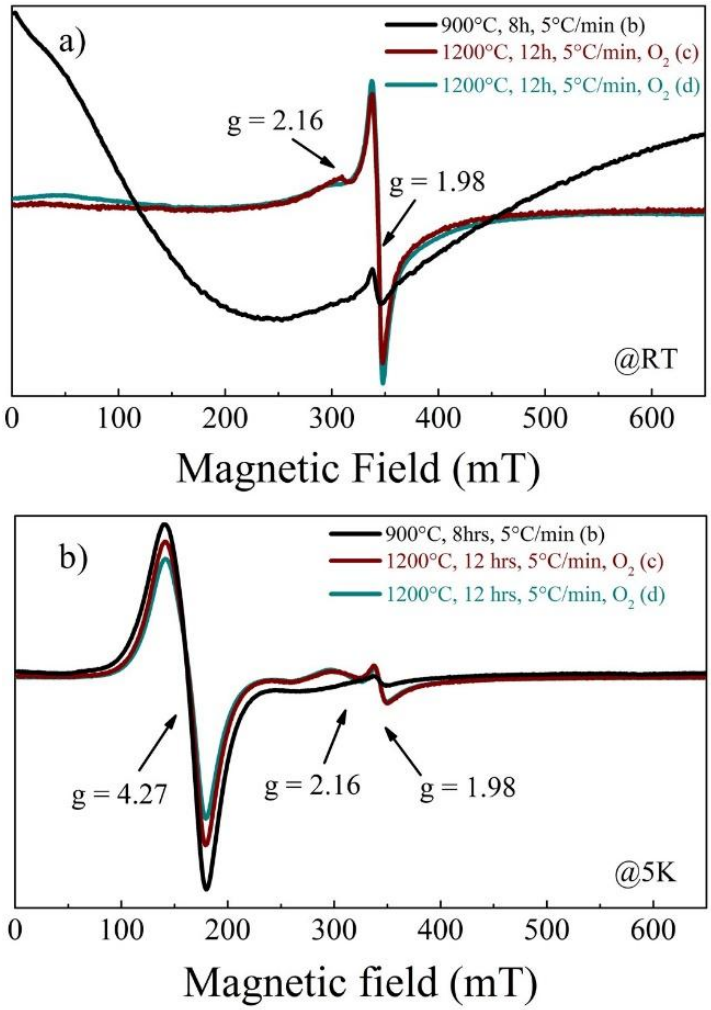

Fig. 11. X-band (~9.5 GHz) Electron Paramagnetic Resonance spectra taken at a) room temperature (RT) and b) 5 K of $Sr_2Co_{0.02}Ga_{0.98}NbO_6$ double perovskite.

In sample b, traces of unreacted Co_3O_4 after the flux step in the sample preparation could have given rise to the broad signal in Fig. 11a. On the contrary, the temperature dependent EPR measurement performed for sample b rules out such hypothesis because no signal at ~280 mT[57] is highlighted when temperature decreases as seen in Fig. S3. Thus, the broad peak suggests an intrinsic paramagnetic signal originated from IS/HS Co^{3+}. When the temperature of the measurement is reduced to 5 K, the slower motion of the electrons weakens the spin-orbit coupling which in turn increases the relaxation time and the broad signal transforms indeed into the two signals at g~4.27 and g~2.16 at 5 K. Interestingly, the intense signal (g~1.98 signal) seen at RT is still observed at 5 K. Its high intensity at RT suggests single trapped electron such as oxygen species following thermal treatments at 1200°C despite the oxygen atmosphere.[51,52]

As pointed out, the g~1.98 may correspond to single trapped electron whereas the two others at g~2.16 and g~4.27 correspond to either Co^{3+} ion in the HS state (S = 2) or in the IS state (S = 1). Due to the broad full width at half maxima of the EPR signals, it is hard to distinguish individually HS and IS spin Co^{3+} signal in the studied double perovskites.

The EPR spectral area gives the content of paramagnetic ions in a sample. As HS/IS Co^{3+} is the mainly paramagnetic ion present in $Sr_2Co_{0.02}Ga_{0.98}NbO_6$ double perovskite if one omits the trapped electrons, the spectral area directly gives the content of HS/IS Co^{3+} ions in the same. The g~1.98 and g~2.16 in the EPR spectra of sample b, c, d have very small contribution to the spectral area, also as the g~4.27 have the same linewidth, it can be easily realized from the spectral area decrease with annealing. This alludes that the amount of HS/IS Co^{3+} in $Sr_2Co_{0.02}Ga_{0.98}NbO_6$ double perovskite is decreasing with annealing which in turn implies that the content of LS Co^{3+} in the sample is increasing. This increase in LS Co^{3+} content indicate that the thermally induced thermochromism may increases with annealing in $Sr_2Co_{0.02}Ga_{0.98}NbO_6$ double perovskite.

III. Room temperature UV-vis-NIR spectroscopy

So as to confirm the presence of mixed spin state of Co^{3+} (LS+IS/HS) as observed from EPR and NMR spectroscopy, UV-vis-NIR spectroscopy technique was made use of. Kulbeka-Munk transformed plot (K/S vs. wavelength where K is the absorption coefficient, S is the scattering coefficient calculated from the diffuse reflectance (R) of the opaque powder used[58]) was used to label the different oxygen to metal charge transfer bands and d-d transitions of Co^{3+}. Fig. 12 shows the Kulbeka-Munk transformed UV-vis-NIR absorption spectra in the range of 200 nm – 1000 nm of undoped sample (sample a) and $Sr_2Co_{0.02}Ga_{0.98}NbO_6$ double perovskite after two annealing processes (sample d).

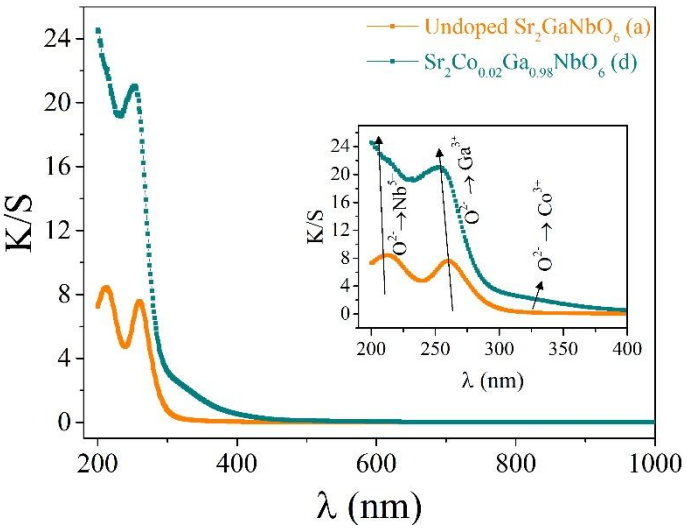

Fig. 12. Room temperature K/S transformed plot (UV-vis-NIR range) of Sr_2GaNbO_6 (sample a) and $Sr_2Co_{0.02}Ga_{0.98}NbO_6$ double perovskite after two annealing processes (sample d).

The inset of Fig. 12 shows the zoomed part of absorption spectra from 200 nm – 380 nm where the arrows are indicator of the oxygen-to-metal charge transfer observed in these samples. The charge transfer band corresponding to the $O^{2-} \rightarrow Nb^{5+}$ have a maximum in the absorption curve in the wavelength range less than 200 nm and the observance of maximum getting to reduce is only visible in the recorded UV-vis-NIR spectra. The charge transfer bands are observed with an onset from ~250 nm corresponding to $O^{2-} \rightarrow Ga^{3+}$ and ~330 nm to $O^{2-} \rightarrow Co^{3+}$. The d-d transitions are poor in intensity in contrast to the Co-doped $LaGaO_3$ perovskite that was showing clear d-d transition peaks corresponding to the LS Co^{3+} at ~500 nm and ~700 nm and to the HS Co^{3+} at ~550 nm.[11] However, as there is a mixture of LS+HS/IS Co^{3+} in sample d under study, the d-d transition peaks might overlap herein which result in indistinguishable maxima making the assignment of peaks to the proper d-d transitions a difficult task. Hence, the second derivative of K/S spectra from 400 nm – 700 nm was calculated to label the d-d transitions corresponding to different Co^{3+} spin states.

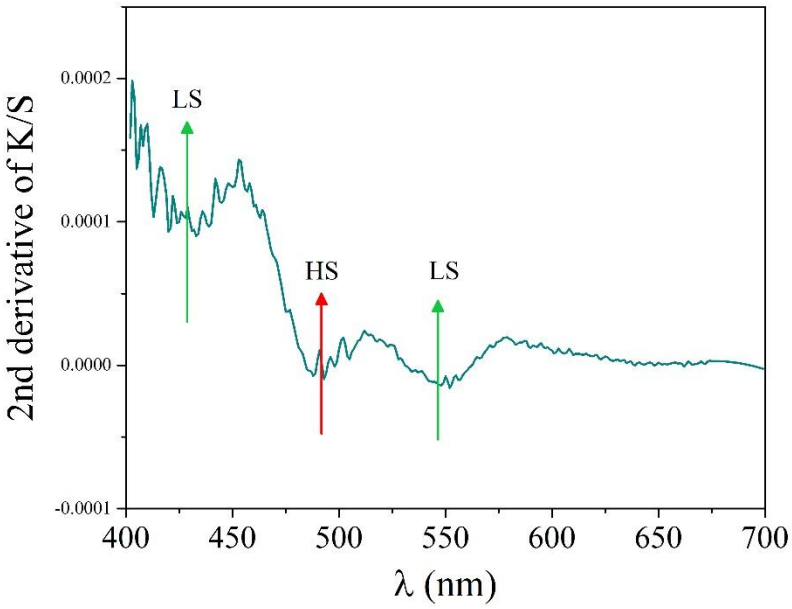

Fig. 13. Second derivative of K/S transformed plot of $Sr_2Co_{0.02}Ga_{0.98}NbO_6$ double perovskite (sample d). Green arrows correspond to the d-d transition of LS Co^{3+} and red arrow to the HS Co^{3+}.

Fig. 13 shows the second derivative plot of K/S transformed plot of light used (400 nm – 700 nm) for the recording of spectra of $Sr_2Co_{0.02}Ga_{0.98}NbO_6$ double perovskite (sample d). d-d transitions which give maxima in UV-vis-NIR spectra (Gaussian peaks) will give minima in second derivative. The analysis of second derivative plot of UV-vis-NIR spectra using Tanabe-Sugano diagram for d^6 electronic configuration resulted in the so assigned d-d transition peaks in Fig. 13 and calculation is tabulated in Table S1. It was seen that the $Sr_2Co_{0.02}Ga_{0.98}NbO_6$ double perovskite has LS, IS and HS Co^{3+} present. The allowed d-d transitions $^1A_{1g} \rightarrow {}^1T_{1g}$ (~547 nm), $^1A_{1g} \rightarrow {}^1T_{2g}$ (~430 nm) corresponding to LS Co^{3+} and the allowed d-d transition $^5T_{2g} \rightarrow {}^5E$ (~490

nm) corresponding to the HS Co^{3+} will give three weak minima in the absorption spectra well identified and located, thanks to the second derivative plot.[59] The final assignment of d-d transitions can be doubtful due to the strong alignment. But anyway, the LS Co^{3+} d-d transitions assignment led to Racah parameter, B and crystal field value, Δ_0 equal to 475 cm^{-1} and 1.5 eV about respectively. These values are coherent with the previous results reported in literature for Co-doped $LaGaO_3$.[11] Furthermore, the weak minima in second derivative plot of K/S at ~645 nm might be a suggestion of $^3T_2$ state (IS Co^{3+}) likely related to oxygen vacancies as observed in $LaCoO_3$[60] nanoparticles or in Lithium-Over stoichiometric $LiCoO_2$[52]. This underpins the observance of HS/IS Co^{3+} from the EPR result and LS from NMR result. Moreover, the non-observance of maxima in the absorption spectra is a sign of: (1) the mixed LS+IS/HS Co^{3+}, (2) different crystal fields due to the occupation of Co^{3+} in the ordered and disordered phases. UV-vis-NIR spectroscopy result reinforces the results obtained from PXRD, EPR and NMR.

Conclusion

In conclusion, our $SrCl_2$ flux synthesis strategy allows us to stabilize at relatively low temperature i.e., 900°C with respect to conventional solid-state route complex refractory perovskite showing B-site ordering. Our combined powder X-ray diffraction and spectroscopic (^{93}Nb, ^{71}Ga and ^{59}Co NMR and EPR) analysis support Ga substitution by Co within the same crystallographic site with a mixed diamagnetic (from ^{59}Co NMR signal that is improved via further annealing process) and paramagnetic (from EPR signal that is impaired via further annealing process) cobalt state stabilization at room temperature in $Sr_2Co_{0.02}Ga_{0.98}NbO_6$ double perovskite. Our samples showed a complex room temperature UV-vis-NIR spectra with less intense d-d transition in contrast to the Co-doped $LaGaO_3$ perovskite further supported a mixed Co^{3+} spin state. Thermochromism property may be induced thermally in these materials under study (which needs to be studied using a chemical selective probe) when comparing with the as reported Co-doped $LaGaO_3$ in which thermochromism was induced between room temperature and 500°C, via spin-crossover of Co^{3+} ion with a change from light to dark brown color.[11] $Sr_2Co_{0.02}Ga_{0.98}NbO_6$ double perovskite with pale brown in color is a possible candidate for the use of inorganic "cool" pigments as the absorption in the UV-vis-NIR spectra in the NIR range is very low. Our material also has the scope of using in roofing tiles or in paints to mediate the indoor temperatures in temperate zones as the reported $AFeO_3$ (A = Ln, Y) brownish inorganic pigments.[61]

Supporting Information

Supporting Information is available for:-

1) Comparison of the XRD patterns obtained for a sample synthesized by combining a precursory ball milling step with the flux method (Flux + B-M) and a sample synthesized with just the flux method (Flux, no B-M)
2) Deconvoluted Nb, ^{71}Ga & ^{59}Co MAS NMR spectra of sample d and deconvoluted ^{71}Ga MAS NMR spectra of sample c & d
3) Temperature dependent EPR spectra of sample b
4) Calculation of the d-d transitions corresponding to the LS and HS Co^{3+} (d^6) using Tanabe-Sugano diagram

Acknowledgement

Authors would like to acknowledge Dr. Dany Carlier for the discussion on NMR spectra.

Maneesha Varghese and Dr. Olivier Toulemonde would like to thank University of Bordeaux for the funding of PhD work. Dr. Struan Simpson and Dr. Gaynor Lawrence thank Erasmus+ training program for their Masterstudent exchange opportunity.

References

(1) Shackelford, J. F.; Doremus, R. H. *Ceramic and Glass Materials: Structure, Properties and Processing*; Springer Science & Business Media: New York, 2008.

(2) Lazaroff, W.; Raschdorf, A. Thermochromic Cookware. Patent number US20060081639A1, April 20, 2006.

(3) Pimia, J. Temperature Indicator for Temperature Changing Material or Means and Method for Its Preparation. Patent number US20130010827A1, January 10, 2013.

(4) Wang, X.; Mu, B.; Xu, J.; Wang, A. Reversible Thermochromic Superhydrophobic $BiVO_4$ Hybrid Pigments Coatings with Self-Cleaning Performance and Environmental Stability Based on Kaolinite. *ACS Appl. Mater. Interfaces* **2021**, *13* (2), 3228–3236.

(5) Cao, L.; Fang, L.; Li, X.; Chen, S.; Lu, C.; Xu, Z. Chameleon Inspired Layer-by-Layer Assembly of Thermochromic Microcapsules to Achieve Controllable Multiple-Color Change. *Smart Mater. Struct.* **2020**, *29* (4), 04LT02.

(6) Liu, X.; Staubitz, A.; Gesing, T. M. Thermochromic Behavior of Yttrium-Substituted Bismuth Oxides. *ACS Appl. Mater. Interfaces* **2019**, *11* (36), 33147–33156.

(7) Heikes, R. R.; Miller, R. C.; Mazelsky, R. Magnetic and Electrical Anomalies in $LaCoO_3$. *Physica* **1964**, *30* (8), 1600–1608.

(8) Blasse, G. Magnetic Properties of Mixed Metal Oxides Containing Trivalent Cobalt. *J. Appl. Phys.* **1965**, *36* (3), 879–883.

(9) Raccah, P. M.; Goodenough, J. B. First-Order Localized-Electron to Collective-Electron Transition in $LaCoO_3$. *Phys. Rev.* **1967**, *155* (3), 932–943.

(10) Naiman, C. S.; Gilmore, R.; DiBartolo, B.; Linz, A.; Santoro, R. Interpretation of the Magnetic Properties of $LaCoO_3$. *J. Appl. Phys.* **1965**, *36* (3), 1044–1045.

(11) Toulemonde, O.; Devoti, A.; Rosa, P.; Guionneau, P.; Duttine, M.; Wattiaux, A.; Lebraud, E.; Penin, N.; Decourt, R.; Fargues, A. et al. Probing Co- and Fe-Doped $LaMO_3$ (M = Ga, Al) Perovskites as Thermal Sensors. *Dalton Trans.* **2018**, *47* (2), 382–393.

(12) Sanz-Ortiz, M. N.; Rodríguez, F.; Rodríguez, J.; Demazeau, G. Optical and Magnetic Characterisation of Co^{3+} and Ni^{3+} in $LaAlO_3$: Interplay between the Spin State and Jahn–Teller Effect. *J. Phys. Condens. Matter* **2011**, *23* (41), 415501.

(13) V, A.; Dogra, A.; Gupta, A.; Pulikkotil, J. J. Retentivity of Spin State Transitions in $LaCoO_3$ with Chemical Disorder. *RSC Adv.* **2015**, *6* (2), 1403–1407.

(14) Gütlich, P.; Gaspar, A. B.; Garcia, Y. Spin State Switching in Iron Coordination Compounds. *Beilstein J. Org. Chem.* **2013**, *9* (1), 342–391.

(15) Buch, V. R.; Chawla, A. K.; Rawal, S. K. Review on Electrochromic Property for WO_3 Thin Films Using Different Deposition Techniques. *Mater. Today: Proc.* **2016**, *3* (6), 1429–1437.

(16) Guo, J.; Guo, X.; Sun, H.; Xie, Y.; Diao, X.; Wang, M.; Zeng, X.; Zhang, Z.-B. Unprecedented Electrochromic Stability of A-WO_{3-x} Thin Films Achieved by Using a Hybrid-Cationic Electrolyte. *ACS Appl. Mater. Interfaces* **2021**, *13* (9), 11067–11077.

(17) Besnardiere, J.; Ma, B.; Torres-Pardo, A.; Wallez, G.; Kabbour, H.; González-Calbet, J. M.; Von Bardeleben, H. J.; Fleury, B.; Buissette, V.; Sanchez, C.et al. Structure and Electrochromism of Two-Dimensional Octahedral Molecular Sieve h'-WO_3. *Nat Commun* **2019**, *10* (1), 327.

(18) Wang, Z.; Wang, X.; Cong, S.; Chen, J.; Sun, H.; Chen, Z.; Song, G.; Geng, F.; Chen, Q.; Zhao, Z. Towards Full-Colour Tunability of Inorganic Electrochromic Devices Using Ultracompact Fabry-Perot Nanocavities. *Nat Commun* **2020**, *11* (1), 302.

(19) Iida, Y.; Kaneko, Y.; Kanno, Y. Fabrication of Pulsed-Laser Deposited V_2O_5 Thin Films for Electrochromic Devices. *J. Mater. Process. Techol.* **2008**, *1–3* (197), 261–267.

(20) Mjejri, I.; Gaudon, M.; Song, G.; Labrugère, C.; Rougier, A. Crystallized V_2O_5 as Oxidized Phase for Unexpected Multicolor Electrochromism in V_2O_3 Thick Film. *ACS Appl. Energy Mater.* **2018**, *1* (6), 2721–2729.

(21) Tong, Z.; Lv, H.; Zhang, X.; Yang, H.; Tian, Y.; Li, N.; Zhao, J.; Li, Y. Novel Morphology Changes from 3D Ordered Macroporous Structure to V2O5 Nanofiber Grassland and Its Application in Electrochromism. *Sci Rep* **2015**, *5* (1), 16864.
(22) Mjejri, I.; Rougier, A.; Gaudon, M. Low-Cost and Facile Synthesis of the Vanadium Oxides V_2O_3, VO_2, and V_2O_5 and Their Magnetic, Thermochromic and Electrochromic Properties. *Inorg. Chem.* **2017**, *56* (3), 1734–1741.
(23) Mjejri, I.; Gaudon, M.; Song, G.; Labrugère, C.; Rougier, A. Crystallized V_2O_5 as Oxidized Phase for Unexpected Multicolor Electrochromism in V_2O_3 Thick Film. *ACS Appl. Energy Mater.* **2018**, *1* (6), 2721–2729.
(24) Liu, X.; Zeng, J.; Yang, H.; Zhou, K.; Pan, D. V_2O_5-Based Nanomaterials: Synthesis and Their Applications. *RSC Adv.* **2018**, *8* (8), 4014–4031.
(25) He, T.; Ma, Y.; Cao, Y.; Yang, W.; Yao, J. Improved Photochromism of WO_3 Thin Films by Addition of Au Nanoparticles. *Phys. Chem. Chem. Phys.* **2002**, *4* (9), 1637–1639.
(26) Bourdin, M.; Salek, G.; Fargues, A.; Messaddeq, S.; Messaddeq, Y.; Cardinal, T.; Gaudon, M. Investigation on the Coloring and Bleaching Processes of WO_{3-x} Photochromic Thin Films. *J. Mater. Chem. C* **2020**, *8* (27), 9410–9421.
(27) Evdokimova, O. L.; Kusova, T. V.; Ivanova, O. S.; Shcherbakov, A. B.; Yorov, Kh. E.; Baranchikov, A. E.; Agafonov, A. V.; Ivanov, V. K. Highly Reversible Photochromism in Composite WO_3/Nanocellulose Films. *Cellulose* **2019**, *26* (17), 9095–9105.
(28) Bechinger, C.; Wirth, E.; Leiderer, P. Photochromic Coloration of WO_3 with Visible Light. *Appl. Phys. Lett.* **1996**, *68* (20), 2834–2836.
(29) Robertson, L. C.; Gaudon, M.; Jobic, S.; Deniard, P.; Demourgues, A. Investigation of the First-Order Phase Transition in the $Co_{1-x}Mg_xMoO_4$ Solid Solution and Discussion of the Associated Thermochromic Behavior. *Inorg. Chem.* **2011**, *50* (7), 2878–2884.
(30) Blanco-Gutierrez, V.; Demourgues, A.; Toulemonde, O.; Wattiaux, A.; Nguyen, O.; Gaudon, M. Understanding the Relationships between Structural Features and Optical/Magnetic Properties When Designing $Fe_{1-x}Mg_xMoO_4$ as Piezochromic Compounds. *Inorg. Chem.* **2015**, *54* (5), 2176–2184.
(31) Blanco-Gutierrez, V.; Demourgues, A.; Gaudon, M. Sub-Micrometric β-$CoMoO_4$ Rods: Optical and Piezochromic Properties. *Dalton Trans.* **2013**, *42* (37), 13622–13627.
(32) Suntivich, J.; May, K. J.; Gasteiger, H. A.; Goodenough, J. B.; Shao-Horn, Y. A Perovskite Oxide Optimized for Oxygen Evolution Catalysis from Molecular Orbital Principles. *Science* **2011**, *334* (6061), 1383–1385.
(33) Grimaud, A.; May, K. J.; Carlton, C. E.; Lee, Y.-L.; Risch, M.; Hong, W. T.; Zhou, J.; Shao-Horn, Y. Double Perovskites as a Family of Highly Active Catalysts for Oxygen Evolution in Alkaline Solution. *Nat Commun* **2013**, *4* (1), 2439.
(34) Maitra, U.; Naidu, B. S.; Govindaraj, A.; Rao, C. N. R. Importance of Trivalency and the e_g^1 Configuration in the Photocatalytic Oxidation of Water by Mn and Co Oxides. *Proc. Natl. Acad. Sci. U.S.A.* **2013**, *110* (29), 11704–11707.
(35) Korotin, M. A.; Ezhov, S. Yu.; Solovyev, I. V.; Anisimov, V. I.; Khomskii, D. I.; Sawatzky, G. A. Intermediate-Spin State and Properties of $LaCoO_3$. *Phys. Rev. B* **1996**, *54* (8), 5309–5316.
(36) Ou, X.; Fan, F.; Li, Z.; Wang, H.; Wu, H. Spin-State Transition Induced Half Metallicity in a Cobaltate from First Principles. *Appl. Phys. Lett.* **2016**, *108* (9), 092402.
(37) Haverkort, M. W.; Hu, Z.; Cezar, J. C.; Burnus, T.; Hartmann, H.; Reuther, M.; Zobel, C.; Lorenz, T.; Tanaka, A.; Brookes, N. B. et al. Spin State Transition in LaCoO3 Studied Using Soft X-Ray Absorption Spectroscopy and Magnetic Circular Dichroism. *Phys. Rev. Lett.* **2006**, *97* (17), 176405.
(38) Haw, S. C.; Hu, Z.; Lin, H. J.; Lee, J. M.; Ishii, H.; Hiraoka, N.; Meléndez-Sans, A.; Komarek, A. C.; Tjeng, L. H.; Chen, K. et al. Unusual Mixed Spin-State of Co^{3+} in the Ground State of $LaSrCoO_4$: Combined High-Pressure and High-Temperature Study. *J. Alloys Compd.* **2021**, *862*, 158050.

(39) Woodward, P.; Hoffmann, R.-D.; Sleight, A. W. Order-Disorder in $A_2M^{3+}M^{5+}O_6$ Perovskites. *J. Mater. Res.* **1994**, *9* (8), 2118–2127.
(40) Iwakura, H.; Einaga, H.; Teraoka, Y. Relationship between Cation Arrangement and Photocatalytic Activity for Sr−Al−Nb−O Double Perovskite. *Inorg. Chem.* **2010**, *49* (24), 11362–11369.
(41) Rietveld, H. M. A Profile Refinement Method for Nuclear and Magnetic Structures. *J. Appl. Crystallogr.* **1969**, *2* (2), 65–71.
(42) Mitchell, R. H. *Perovskites: Modern and Ancient*; Almaz Press: Thunder Bay, Ontario, 2002.
(43) Vasala, S.; Karppinen, M. $A_2B'B''O_6$ Perovskites: A Review. *Prog. Solid State Chem.* **2015**, *43* (1–2), 1–36.
(44) Glazer, A. M. The Classification of Tilted Octahedra in Perovskites. *Acta Crystallogr. B Struct. Cryst. Cryst. Chem.* **1972**, *28* (11), 3384–3392.
(45) Alonso, J. A.; Martínez-Lope, M. J.; Casais, M. T.; Fernández-Díaz, M. T. Evolution of the Jahn−Teller Distortion of MnO_6 Octahedra in $RMnO_3$ Perovskites (R = Pr, Nd, Dy, Tb, Ho, Er, Y): A Neutron Diffraction Study. *Inorg. Chem.* **2000**, *39* (5), 917–923.
(46) Lufaso, M. W.; Woodward, P. M. Jahn-Teller Distortions, Cation Ordering and Octahedral Tilting in Perovskites. *Acta Crystallogr. B Struct. Sci.* **2004**, *B60*, 10–20.
(47) Barnes, P. W.; Lufaso, M. W.; Woodward, P. M. Structure Determination of $A_2M^{3+}TaO_6$ and $A_2M^{3+}NbO_6$ Ordered Perovskites: Octahedral Tilting and Pseudosymmetry. *Acta Crystallogr. B Struct. Sci.* **2006**, *62* (3), 384–396.
(48) Sleight, A. W. A Study of the Incidence of the Ordered Perovskite Structure. Ph.D. Dissertation, Inorganic chemistry, University of Connecticut, Connecticut, 1963.
(49) N. Hooper, T. J.; A. Partridge, T.; J. Rees, G.; S. Keeble, D.; A. Powell, N.; E. Smith, M.; P. Mikheenko, I.; E. Macaskie, L.; T. Bishop, P.; V. Hanna, J. Direct Solid State NMR Observation of the ^{105}Pd Nucleus in Inorganic Compounds and Palladium Metal Systems. *Phys. Chem. Chem. Phys.* **2018**, *20* (41), 26734–26743.
(50) Massiot, D.; Messinger, R. J.; Cadars, S.; Deschamps, M.; Montouillout, V.; Pellerin, N.; Veron, E.; Allix, M.; Florian, P.; Fayon, F. Topological, Geometric, and Chemical Order in Materials: Insights from Solid-State NMR. *Acc. Chem. Res.* **2013**, *46* (9), 1975–1984.
(51) Duffiet, M.; Blangero, M.; Cabelguen, P. E.; Song, K. S.; Fauth, F.; Delmas, C.; Carlier, D. Probing Al Distribution in $LiCo_{0.96}Al_{0.04}O_2$ Materials Using ^{7}Li, ^{27}Al, and ^{59}Co MAS NMR Combined with Synchrotron X-Ray Diffraction. *Inorg. Chem.* **2020**, *59* (5), 2890–2899.
(52) Levasseur, S.; Ménétrier, M.; Shao-Horn, Y.; Gautier, L.; Audemer, A.; Demazeau, G.; Largeteau, A.; Delmas, C. Oxygen Vacancies and Intermediate Spin Trivalent Cobalt Ions in Lithium-Overstoichiometric $LiCoO_2$. *Chem. Mater.* **2003**, *15* (1), 348–354.
(53) Areán, C. O.; Delgado, M. R.; Montouillout, V.; Massiot, D. Synthesis and Characterization of Spinel-Type Gallia-Alumina Solid Solutions. *Z. Anorg. Allg. Chem.* **2005**, *631* (11), 2121–2126.
(54) Cook, D. S.; Hooper, J. E.; Dawson, D. M.; Fisher, J. M.; Thompsett, D.; Ashbrook, S. E.; Walton, R. I. Synthesis and Polymorphism of Mixed Aluminum–Gallium Oxides. *Inorg. Chem.* **2020**, *59* (6), 3805–3816.
(55) Wang, X.; Huang, K.; Yuan, L.; Li, S.; Ma, W.; Liu, Z.; Feng, S. Molten Salt Flux Synthesis, Crystal Facet Design, Characterization, Electronic Structure, and Catalytic Properties of Perovskite Cobaltite. *ACS Appl. Mater. Interfaces* **2018**, *10* (33), 28219–28231.
(56) Ivanova, S.; Zhecheva, E.; Stoyanova, R. Microstructure of $LaCoO_3$ Prepared by Freeze-Drying of Metal–Citrate Precursors Revealed by EPR. *J. Phys. Chem. Solids* **2007**, *68* (2), 168–174.
(57) Mesaros, A.; Ghitulica, C. D.; Popa, M.; Mereu, R.; Popa, A.; Petrisor, T.; Gabor, M.; Cadis, A. I.; Vasile, B. S. Synthesis, Structural and Morphological Characteristics, Magnetic and Optical Properties of Co Doped ZnO Nanoparticles. *Ceram. Int.* **2014**, *40* (2), 2835–2846.
(58) Kubelka, P.; Munk, F. An Article on Optics of Paint Layers. *Z. Physik* **1931**, *12*, 593–601.

(59) Sanz-Ortiz, M. N.; Rodríguez, F.; Demazeau, G. Spin Transition in Co^{3+} by Optical Absorption and Time-Resolved Spectroscopy under Pressure: An Appraisal of the Different Spin States. *High Press. Res.* **2008**, *28* (4), 571–576.
(60) Zhou, S.; Shi, L.; Zhao, J.; He, L.; Yang, H.; Zhang, S. Ferromagnetism in $LaCoO_3$ Nanoparticles. *Phys. Rev. B* **2007**, *76* (17), 172407.
(61) Fortuño-Morte, M.; Serna-Gallén, P.; Beltrán-Mir, H.; Cordoncillo, E. A New Series of Environment-Friendly Reddish Inorganic Pigments Based on $AFeO_3$ (A = Ln, Y) with High NIR Solar Reflectance. *J. Materiomics* **2021**, *7* (5), 1061–1073.